JPL D-6846

Distribution Category
UC-93

ECUT
Energy Conversion and Utilization Technologies Program

Direct Conversion Technology

JPL-D--6846

DE90 010057

Annual Summary Report CY 1989

Prepared by:

Paul F. Massier
and by
C. P. Bankston, R. Williams, M. Underwood,
B. Jeffries-Nakamura, and G. Fabris
Jet Propulsion Laboratory
California Institute of Technology

December 4, 1989

Sponsored by

Energy Conversion and Utilization Technologies Program
Office of Energy Utilization Research
U.S. Department of Energy
Washington, D.C. 20585

Through an agreement with

National Aeronautics and
Space Administration

by

Jet Propulsion Laboratory
California Institute of Technology
Pasadena, California

Prepared by the Jet Propulsion Laboratory, California Institute of Technology, for the U.S. Department of Energy through an agreement with the National Aeronautics and Space Administration.

The work reported herein was performed through NASA Task RE-152, Amendment 308, and was sponsored by the U.S. Department of Energy under IAA DE-AI01-86CE90237.

TABLE OF CONTENTS

LIST OF FIGURES

SUMMARY

The overall objective of the Direct Conversion Technology task is to develop an experimentally verified technology base for promising direct conversion systems that have potential application for energy conservation in the end-use sectors.

This report contains progress of research on the Alkali Metal Thermal-to-Electric Converter (AMTEC), and on the Two-Phase Liquid-Metal MHD Electrical Generator (LMMHD) for the period January 1, 1989 through December 31, 1989. Research on these concepts was initiated during October 1987. Reports prepared on previous occasions (Refs. 1, 2, and 3) contain discussions on the following other direct conversion concepts: thermoelectric, pyroelectric, thermionic, thermophotovoltaic, thermoacoustic, thermomagnetic, thermoelastic (nitinol heat engines); and also, more complete discussions of AMTEC and LMMHD systems.

Research on the Alkali Metal Thermal-to-Electric Converter (AMTEC) during this period has proceeded in three major areas:

1. Improvements in electrode modeling have resulted in a comprehensive description of electrode performance under constant load; and investigation of the frequency and temperature dependencies of electrodes' responses has provided both additional evidence supporting the basic model, and additional information about the interfacial capacitance and transport modes such as surface diffusion. Work in support of the Westinghouse AMTEC effort has included the collaborative application of modeling results to AMTEC systems studies.

2. With the help of these studies, evaluation and optimization of advanced electrodes, including rhodium-tungsten (Rh/W), which has demonstrated stable power densities of ~0.7 W/cm^2 at 1200 K, and titanium nitride (TiN) has proceeded. Work in support of the Beta Power, Inc. AMTEC effort has included evaluation of their TiN electrodes at JPL and will soon include preparation of Rh/W electrodes for evaluation in their vapor-fed recirculating cell. The Pt/W and Rh/W electrodes are the most promising electrodes investigated so far, with

both high power and stability. However, the TiN electrode system is, at this time, less optimized, and remains a viable backup candidate.

3. The recirculating test cell (RTC) has demonstrated all operational functions at acceptable performance levels and several high temperature tests, including a 290 hour test at $T \geq 1050$ K, with good electrode performance from thin Mo electrodes, and successful thermal characterization of the cell.

Research on the Two-Phase Liquid-Metal MHD Electrical Generator is focused on the reduction of slip between the gas bubbles and the liquid metal during the expansion process in the MHD electrical generator. Air and water mixes with the addition of surface active agents (surfactants) are being investigated to determine the factors that control mixture uniformity and prevention of bubble coalescence. The knowledge gained from these experiments is being used to design and construct the mixing section of a liquid-metal and a gas MHD generator blowdown system which will be used for conducting experiments with actual system working fluids such as NaK and N_2.

A matrix of 18 tests at different combinations of air (or nitrogen) and water mixes have been performed with and without surfactants (soap). It has been observed with the aid of ordinary and x-ray photographs that with a surfactant flow rate in the range of 0.01 to 0.1 per cent of water flow rate the coalescence of bubbles, due to their collisions or touching, was prevented. Furthermore, there were dramatic differences in bubble diameter for air-water mixes alone as compared to mixes with a surfactant. For air-water alone bubble diameter was between 2 and 3 millimeters; whereas, with surfactant the diameter was about one-tenth the size, 0.2 to 0.3 millimeters. Thus, there was about one thousand times more bubbles in the flows with surfactant.

Digital processing of x-ray images taken of the air/water mixed flows produced results which indicated that for one pair of experiments with the same air and water flowrates the average void fraction with surfactant added was 0.8; whereas, without surfactant added the void fraction was only 0.55. These values translate into velocity slip ratio of 1.2 with surfactant flow but a much larger

(worse) slip ratio of 4.1 without surfactant flow. This illustrates the benefit attainable with surfactant in achieving low slip at high void fraction.

Preliminary design of various liquid-metal blowdown system components has been completed.

A. INTRODUCTION

A comprehensive introduction to the Direct Conversion Technologies activities appears in Ref. 1. Descriptions of various direct thermal-to-electric conversion systems appear in Refs. 1-3. The systems described are: Alkali Metal Thermal-to-Electric Converter (AMTEC), Two-Phase Liquid Metal MHD (LMMHD) Electrical Generator, Thermoelectric, Thermionic, Pyroelectric, Thermoacoustic, Thermoelastic (Nitinol heat engine), Thermophotovoltaic, and a variety of Thermomagnetic concepts. Assessments of these systems have been made and research needs have been identified for systems which, if developed, appear to show promise for energy conservation in the end-use sector. Initially, two systems were selected for exploratory research and advanced development. These are AMTEC and LMMHD. This report presents progress that has been made during CY 1989 on research activities associated with these two systems.

B. OBJECTIVES

The overall objective of the direct conversion technology task is to develop an experimentally verified technology base for promising direct conversion systems that have potential application for energy conservation in the end-use sectors. Specific objectives are:

1. For the Alkali Metal Thermal-to-Electric Converter continue the research to increase the lifetime of electrodes by investigating the most promising materials, which consist of molybdenum, tungsten and their alloys. In addition, evaluate titanium nitride electrodes in support of Ford and Beta Power, Inc. AMTEC programs. Also, continue detailed thermal analysis and experimental verification of the AMTEC cycle.

2. For the Two-Phase Liquid-Metal MHD Electrical Generator continue the research to improve the performance of the generator by exploring methods to reduce slip between the expanding gas bubbles and the liquid metal. Also, assemble a system for conducting experiments with a liquid metal based on the understanding gained from the air-water experiments.

3. Continue to examine advanced and innovative direct thermal-to-electric energy conversion concepts, identify those that are promising, determine industrial needs for application (which concept should be used for which industrial need), and determine critical research needs for promising concepts.

C. RESEARCH ACTIVITIES

1. Alkali Metal Thermal-to-Electric Converter (AMTEC)

a. Electrode Technology

During this period, an evaluation of titanium nitride (TiN) electrodes has been initiated in partial support of the Ford/ERIM and Beta Power, Inc. AMTEC programs. Investigations at those two laboratories have found that TiN electrodes have long lifetime potential at moderate power densities (about 0.5 W/cm^2). The JPL study is utilizing beta"-alumina solid electrolyte (BASE) tubes with TiN electrodes deposited by a proprietary process at Beta Power, Inc. The objective is to gain an understanding of and model transport mechanisms for these electrodes, utilizing JPL developed electrochemical analytical techniques not otherwise available at other laboratories. Presumably, accurate performance modeling and a basis for possible optimization will be the result.

A comprehensive titanium nitride (TiN) experiment was carried out in the electrode test cell. The electrodes were deposited by Beta Power, Inc. on a 0.7 mm wall-thickness BASE tube, compared with the 1.2 mm thick BASE tubes usually used. The electrodes were approximately 20 microns thick; much thicker than molybdenum or platinum-group tungsten electrodes (usually 0.5-5 μm). These electrodes produced 0.4 W/cm^2 in the range 1135-1185 K, and slowly decayed to about 0.3 W/cm^2 after 78 hours.

A second experiment at similar temperatures with partially optimized TiN electrodes of average thickness ~5.0 μm on an older 1.2 mm thick walled BASE tube gave somewhat lower power densities, ~0.3 W/cm^2 from the larger, 4.7 cm^2, electrodes, but higher power densities, ~0.5 W/cm^2, from the small, 1.0 cm^2,

electrodes. Analysis of the measurements indicates that series resistance, in particular BASE resistance, was responsible for the poor performance of the larger electrodes. The transport properties associated with these electrodes were apparently significantly improved compared with the 20 μm TiN electrodes, but the experiment only operated at high temperature for about 200 hours, so that comprehensive analysis was not possible. Good a.. impedance data and sheet resistance measurements were obtained and data from both experiments suggest some preliminary model characteristics for the TiN electrode performance.

The results of the first TiN experiment (Figures 1 and 2) show that: i) Enhanced transport (compared to vapor diffusion) must be present to give power densities of 0.3 to 0.4 W/cm^2 with 20 μm thick electrodes. The nature of this enhancement is being investigated. Surface diffusion is a candidate. ii) Even so, transport is limiting for such thick electrodes and deposition techniques must be developed to deposit thinner electrodes. Modeling parameters derived from the data show that higher power densities are possible and measured sheet resistances show that thinner electrodes will not result in significant additional iR losses. iii) Slow degradation of power density by a factor of up to two is due either to morphological or chemical changes that are now being studied. The result is that the morphology parameter (G = (electrode thickness)/((pore radius)^3 x (pore area density))) increases with time during the experiment (Figure 2). Assuming that degradation has leveled off at 75 hours, then thinner TiN electrodes in combination with the thinner electrolyte could still stably produce 0.5 W/cm^2. Thus, it is concluded that this electrode system remains a possible backup to platinum-group tungsten electrodes. Thinner TiN electrodes will be studied subsequently in greater detail.

The TiN electrode work was presented at the May 1989 Meeting of the Electrochemical Society, at Los Angeles. A copy of the abstract appears herein as Appendix A.

Several experiments have been carried out in the Electrode Test Cell to further evaluate Rh/W electrodes ranging in thickness from 0.5 to 1.0 μm. The goals of these experiments included correlation of electrode characteristics with performance; more detailed characterization of the temperature dependence

of electrode kinetics and mass transport in these electrodes; improved temperature measurements; and electrode optimization. Most of these electrodes produced stable power densities at maturity (up to 150 hours) of 0.5 W/cm^2, but none were as thick as the best Rh/W electrodes studied previously. It is concluded that these thinner electrodes, while capable of good power densities, have sheet and contact resistances that are too high to be optimum. 1.5-2.0 μm thick electrodes are now estimated to be optimum for this system. Fits to ac impedance data and current voltage curves of mature Rh/W electrodes taken over a range of 928 K to 1213 K allow us to characterize the temperature dependencies of electrochemical kinetics and mass transport in these electrodes. The exchange current shows temperature dependence and values in the same range as thin Mo electrodes. Both of these electrodes show collision frequency dominated kinetics, rather than an activation energy associated with the charge transfer process. However, while mass transport in thin Mo electrodes is characterized by Knudsen flow, with weak ($\sqrt{T}$) temperature dependence, mass transport in Rh/W electrodes shows very strong, reversible temperature dependence. There appears to be an "onset" temperature for enhanced mass transport in the temperature range near 1000 K, with quite favorable transport observed throughout the most useful AMTEC operating range of 1050 to 1250 K. There are good reasons, based on published results as well as model calculations, for ascribing enhanced transport in Rh/W and Pt/W electrodes to rapid surface diffusion of sodium in sub-monolayer coverage on the grain of the intermetallic phases.

In another Rh/W experiment, temperature measurements at the electrode surface were taken in order to determine the temperature gradient through the wall of the BASE. Temperature differences were 10 to 30 K at high temperature. This information can be incorporated in systems calculations of AMTEC performance. Other experiments with W electrodes have indicated that the change in electrode temperature with current flow, dT/dj, is approximately 10 K A^{-1} cm^2. Improvements in accuracy and precision of cell and especially electrode thermal measurements is critical for improved modeling and detailed systems analysis.

A refereed paper entitled, "High Power Density Performance of WPt and WRh Electrodes in the Alkali Metal Thermoelectric Converter," appeared in the

Journal of the Electrochemical Society, Vol. 136, No. 3, March 1989, pp. 893-894. A copy is included as Appendix B.

The electrode kinetics/mass transport model was refined further during the last year. The most important developments have been the characterization and analysis of the temperature dependence of the exchange current in mature Mo electrodes from 740 to 1240 K, in mature Rh/W electrodes from 920 to 1220 K, and preliminary results over a ~200 K range in TiN. This has given significant information about the mechanistic basis of the charge transfer process in these electrodes. Mass transport data has also been derived from the same experimental data: ac impedance under varying dc bias; and current-voltage curves. Finally, detailed analysis of the frequency dependence of the ac impedance data has allowed resolution of the charge transfer/interfacial capacitance component of the ac response from the slower mass transport process, and identification of a Warburg-like diffusion contribution to the mass transport process at higher frequencies in Mo and possibly Rh/W electrodes. The analysis of TiN electrodes is much more complex in that in addition to a moderate to high frequency charge transfer/mass transport process, an additional low frequency mass transport process, which slowly changes with time, has also been identified.

In addition, a refereed paper documenting the electrode modeling work described in Ref. 3, titled, "Mass Transport, Charge Transfer and Ohmic Losses in the Alkali Metal Thermoelectric Converter," appeared in Industrial Chemical Engineering Symposium Series No. 112, The Institution of Chemical Engineers, Rugby, UK, pp. 153-163 (1989). A copy is included as Appendix C. Appendix A also contains a second abstract on the modeling work that was presented at the May 1989 meeting of the Electrochemical Society.

Two additional papers, listed in Appendix C, have been submitted to the Journal of the Electrochemical Society. These are titled "Kinetics and Transport at AMTEC Electrodes, I. The Interfacial Impedance Model," and "Kinetics and Transport at AMTEC Electrodes, II. Temperature Dependence of the Interfacial Impedance of $Na_{(g)}$/Porous Mo/Na^+-Beta"-Alumina" and they describe in detail the investigations described above, except for the more recent results on Rh/W and TiN electrodes.

b. Recirculating Test Cell

The AMTEC recirculating test cell (RTC) has demonstrated all operational functions at required levels for the first time, in a series of high temperature experiments. Required functions included power production: 0.5 W/cm^2 from an Rh/W electrode; sodium circulation: >20 cc/min against 0.5 atmospheres; effective wetting of the condenser resulting in a radiation reduction factor of 16; an area-extrapolated estimated electrode efficiency of 10 to 14% at 1050 K; a reproducible, high quality BASE to niobium or tantalum braze seal; and well behaved feedthrough and lead/current collector configurations. RTC performance was studied at up to 1100 K in two experiments, and one experiment ran 290 hours at temperatures from 1000 to 1100 K. These experiments were a major step toward full operational status for the RTC. One of the earlier of these experiments, along with detailed aspects of cell assembly and operation, is described in Appendix D. This paper appeared in the Proceedings of the Intersociety Energy Conversion Engineering Conference (IECEC) during August of this year.

2. Two-Phase Liquid-Metal MHD Generator (LMMHD)

Research on the Two-Phase Liquid-Metal MHD Electrical Generator is focused on the reduction of slip between the gas bubbles and the liquid metal during the expansion process in the MHD generator. Air (or nitrogen) and water mixes with the addition of surface active agents (surfactants) are being investigated to determine the factors that control mixture uniformity and prevention of bubble coalescence. Efficient generation of electricity in the two phase liquid-metal MHD generator concept requires that this mixture retains a bubbly flow pattern while expanding to a lower pressure in the generator. The expanding gas bubbles "push" the surrounding liquid against the Lorentz force which results from the interaction of the electrically conducting liquid metal with an applied magnetic field.

The approach is to first investigate the factors that control mixture uniformity by conducting designed experiments using air and water with and without the addition of surface active agents (surfactants). Air and water mixtures are used because advancements in understanding mixing and bubble

behavior can be made much more rapidly than by starting directly with a liquid metal. Visual observation is possible and the fluids are safe to use. The most critical factor in simulating the dynamics of gas/liquid metal mixing is prevention of bubble coalescence by surface activity. The formation of bubbles at a gas injection surface is governed by wetting, by buoyancy, and by fluid dynamic drag forces on the bubbles. Use of surface active additives ensures good wetting; however, different additives would be used in the liquid metal system. The buoyancy and drag forces in the mixer and the nozzle are influenced primarily by density and viscosity. Both the density and viscosity of sodium-potassium (NaK) are only 15 percent smaller than corresponding values for water. A significantly higher pressure will exist in the NaK-N_2 mixer which means that the density of the gas will be different; however, the density of the gas plays a negligible role in the bubble flow mixing process.

Once a uniform bubbly mixture has been created in the mixer it is expected that this flow pattern will not change during rapid expansion through the nozzle and the LMMHD generator. This will be facilitated primarily by the presence of a surface active agent creating favorable dynamic surface tension around bubbles. This will induce local flow of gas-liquid interfaces and the associated liquid boundary layer preventing coalescence of bubbles. It is also expected that cooling of the interface by the expanding gas will induce similar dynamic surface tension effects. The planned LMMHD blow-down loop will have a volume expansion ratio of up to 40 which is an order of magnitude higher than any past experiments. The short residence fluid flow time in the nozzle and the LMMHD generator increases the likelihood of preserving the bubbly flow pattern.

G. Wallis (Ref. 4) has performed mixing experiments (pool bubbling) in the past showing that even when strong surfactant is added, a mixer could generate large gas slugs resulting in high gas slip velocity. Basically this is because at high gas injection velocity "hydrodynamic instability" prevents creation of small bubbles, but large gas slugs are generated. There is no reliable experimental data on "critical" gas injection velocities for the case of forced two-phase flow.

Numerous experiments have been conducted at JPL with and without the addition of soap as a surfactant. These mixing experiments have demonstrated high void fractions (with surfactant) of up to 80 percent at the downstream end of the porous injection plates with slip velocity ratio close to unity. For the same air and water flowrates without surfactant the average void fraction was 55 percent with velocity slip ratio of 4.1.

With a surfactant, bubbles are about a thousand times smaller in volume than without surfactant. Thus, smaller bubbles follow curving streamlines much better, thereby maintaining more uniform two-phase flow.

There is also concern about gas separation at the trailing edge of the injection elements. In usual flow configurations there is an adverse pressure gradient at the trailing edge of an element. This causes a large gas separation bubble to attach itself at the trailing edge. This bubble generates other large gas slugs which flow downstream. Our mixing experiments have demonstrated that this problem can be completely eliminated with a wedged trailing edge and contraction of flow crossectional area along the stream. This kind of flow configuration creates a favorable pressure gradient which prevents two-phase separation at the trailing edge.

Additional results of these experiments are discussed in the following sections. The knowledge gained from these results is being used to design and construct the mixing section of a liquid-metal blowdown system which will be used for conducting experiments with actual system working fluids such as NaK and N_2.

a. Air-Water Mixing

(1) Mixing Element

Difficulties were encountered but eventually overcome in manufacturing of the mixing element (Figure 3). Initially the porous plates, per recommendation of the manufacturer, were welded to a stainless steel metal frame by torch welding under inert gas. This was done three times in the JPL Weld Shop.

However, numerous cracks appeared in the porous plate in the vicinity of the welds. Following this, per recommendation of the plate manufacturer, a new frame for the element was sent to the manufacturer in Connecticut for welding. The element that they had welded was leak-tight without any cracks. However, the plates on the element were wave-like (peaks to valleys roughly up to quarter of an inch). This was not satisfactory since it resulted in very nonuniform distribution of the gas injection through the porous plates. The "waviness" of the plates was apparently caused by large heat input during the welding.

In the meantime, JPL's Weld Shop received laser welding equipment. The laser introduces substantially less heat into the welds. Hence, the laser welding equipment was used for all subsequent welding. No distortions of the porous plates were experienced. However, the welds are quite shallow (maximum depth of 0.025 inches) and narrow. Several times, with this and subsequent porous plates, the welds were not deep enough and cracks opened in exactly the middle of the weld. However these cracks were easily rewelded with the laser system.

Another difficulty was encountered with the uniformity of gas injection even when a porous plate was perfectly flat. The plate manufacturer claimed spatial nonuniformity of the rate of injection to be less than 20 percent. However, in actuality the nonuniformity was much greater. At the suggestion of the manufacturer the porous element was cleaned with a solvent solution, and an ultrasonic cleaner was used as well. Also, pure bottled nitrogen was then used for injection instead of shop air. All of this helped to improve uniformity of gas injection, but usually after running an experiment for fifteen minutes the injection nonuniformities would worsen.

In order to resolve the above problems a new injection element which contained a dividing plate inside of the gas injection cavity was made. This allowed gas injection rate on both sides of the element to be adjusted independently. It turned out that this modified element had well-balanced injection rates on both sides without any adjustment. This element had a plate porosity of 0.5 microns and a thickness of 0.047 inches. All remaining gas/water experimental data was taken with this element.

b. Optimization of X-Ray Picture Taking

X-ray pictures were taken of the bubbly flow in the mixing section and in order to obtain better two-dimensionality of x-ray photographs the x-ray source was located as far from the mixing test section as possible. For the same reason the x-ray film was placed as close to the test section (the object) as possible. Source to object distance (STOD) was 14 feet and the object to film distance (OTFD) was 4 inches. Different x-ray films, x-ray charging voltages, and number of x-ray discharges per one x-ray photograph have been tried. As a result of these optimization experiments the following selections have been made: Cronex 4 x-ray film, Kevlar Pediatrics film cassette, two Quanta Fast Detail Intensifying Screens, 275 kV discharge voltage, ten discharges per photo.

In order to be able to reach higher void fraction downstream of the injection element new plexiglas inserts have been used which reduced the downstream flow channel dimension to 1/2" x 4". The present test section dimensions are shown in Figure 3. In the region of the trailing edge of the wedge the flow cross-section decreases along the flow causing acceleration and a favorable pressure gradient. Consequently, there was no separation of two-phase flow at the trailing edge of the element.

c. Processing of X-Ray Negatives

Typical x-ray negatives are shown on Figures 4 and 5. The x-ray negative image of the calibration stepwedge is given in Figure 4. A sketch of the stepwedge in given in Figure 6. The stepwedge simulates the full range of possible void fractions in the test section channel. Its cavity is filled with water. The full channel is four inches wide (in the x-ray direction) plus two half-inch thick plexiglas walls. The bottom of the stepwedge simulates the channel at zero void fraction. The top of the stepwedge corresponds to the 100 percent void fraction condition. Images of the negatives displayed in Figures 4 and 5 were actually taken simultaneously on the same x-ray film. Different shades of light (or darkness) on the stepwedge as seen in Figure 4 correspond to different known calibration levels of the void fractions. Thus, shades of light in Figure 5 can be used to read corresponding void fractions in the test section

channel. In order to remove subjectivity in estimating degrees of shades of the negatives a video camera has been used as a means to accomplish this. The camera can be focused to a small area (as small as two by two millimeters). It is connected to an IBM computer with appropriate software. The output is the average shadiness level as well as a histogram of levels for pixels within the camera viewing area. There are 256 digital shadiness levels. It was necessary to change F-stop a number of times as the camera was moved from one area of calibrated void fraction of the negative to another. Typical calibration curves showing void fractions versus the pixel light level are shown in Figure 7. Five different F-stops were necessary to cover the full range of void fractions. It can be seen that for a particular F-stop there is a very large change of the numerical pixel light level with a small change of void fraction. Thus, void fractions can be read with good accuracy.

d. Measurement of Flow Rates

A turbine flow-meter was used to measure the water flow rate. The calibration of the flow meter was accomplished by measuring the time taken to fill a 55 gallon drum. The data with a line fitted through the data points is shown in Figure 8.

Air-flow rate was obtained using an orifice and the conventional pressure measurements. The orifice was calibrated by blowing air into the inverted large plastic bucket which was placed into a large pan-like container filled with water. Effects of the hydrostatic heads on the volume of air in the bucket were taken into account. A formula for determination of the air flow rate is

$$Q = KA \sqrt{\frac{2}{\rho} (P_1 - P_2)} \quad .$$

K is calibration constant which was determined to be 0.8. A is area of the orifice opening. ρ is density of the gas at the orifice. P_1-P_2 is pressure drop across the orifice.

e. Results

In the flow visualization experiments air and water flow rates were each adjusted at three different levels. Tests were conducted at each of these combinations with and without surfactant flow. This provided a test matrix of 18 different mixing flow cases. Three photographs were made for each of these cases. Two close up photographs of the flow were taken at the trailing edge from two different directions. The third photo was taken from a larger distance. The three levels of water flow rates were 0.25, 0.7, 2.0 liters per second while air (or nitrogen) flow rates were 0.23, 0.5, 1.6 liters per second. All these tests are listed in Table 1. Flow crossectional area downstream of the injection element was 1/2" x 4". All the experiments were done at room temperature. Pressure in the channel adjacent to the injection element was at about 17.7 PSIA (122 x 10^3 N/m^3) due to the hydrostatic head of liquid above this location.

TABLE 1. AIR-WATER MIXING FLOW VISUALIZATION TESTS

TEST NUMBER	AIR FLOWRATE		WATER FLOWRATE	SURFACTANT FLOWRATE
	$\frac{\ell}{s}$	$\frac{g}{s}$	$\frac{\ell}{s}$	$\frac{m\ell}{s}$
1	0.23	0.32	0.25	0
2	0.23	0.32	0.25	0.2
3	0.50	0.70	0.25	0
4	0.50	0.70	0.25	0.2
5	1.60	2.24	0.25	0
6	1.60	2.24	0.25	0.2
7	0.23	0.32	0.70	0
8	0.23	0.32	0.70	0
9	0.50	0.70	0.70	0
10	0.50	0.70	0.70	0.2
11	1.60	2.24	0.70	0
12	1.60	2.24	0.70	0.2
13	0.23	0.32	2.00	0
14	0.23	0.32	2.00	0.2
15	0.50	0.70	2.00	0
16	0.50	0.70	2.00	0.2
17	1.6	2.24	2.00	0
18	1.6	2.24	2.00	0.2

The flow rate of the surfactant (liquid soap) was 0.01 to 0.1 percent of the flow rate of water. This was sufficient to induce strong surface activity and prevent coalescence of bubbles due to their collisions or touching. If the concentration of a surfactant exceeds the concentration of maximum reduction of surface tension (about 0.002 per cent for soap in water) then its effect on prevention of bubble coalescence is quantitively independent of the actual concentration. However, the surface activity cannot completely prevent formation of large gas bubbles on the porous plates if the local gas injection velocity is too high. Observations indicate that surface activity does help to postpone transition from small bubbles to patchy (large bubbles) gas injection. The transition occurs at somewhat higher injection rates. Due to nonuniformity of local pressure drop across the porous plate the transition to the patchy gas injection occurred first at only a few locations. This made it difficult to ascertain quantitatively the effect of the surface activity on the critical injection rate.

Figures 9 and 10 show two-phase flow around and immediately downstream of the trailing edge of the injection element. Air and water flow rates were low and the same for the tests shown in both Figures. The only difference between them is that a small amount of liquid surfactant (soap) was used for the tests shown in Figure 10. Dramatic difference can be observed. For air and water alone (Figure 9) the bubbles are 2 to 3 millimeters in diameter. In the case of soap addition the bubbles are much smaller. Close visual observations indicate that these bubbles are about 0.2 to 0.3 millimeters in diameter. In other words, there were about a thousand times more bubbles in the test with surfactant than without surfactant. It is suspected that this is caused mainly by better wetting of the injection pores by the surfactant solution. In this way the neck of the growing bubbles is much thinner resulting in much smaller detaching bubbles. It is also possible that in the surfactant flow case number of very small bubbles coalescence while growing on the injection surface. In such a way larger (2 to 3 mm) bubbles could be formed before detachment. In the surfactant case no such coalescence occurs.

Perpendicular views of the same two tests are given in Figures 11 and 12. The size of the bubbles can now be seen even better. The white portion in the

central part of these two photographs was a cavity pocket in front of the channel which became filled with air bubbles, especially when surfactant was used. This portion of the photographs should be disregarded.

Figures 13 and 14 show the entire channel for non-surfactant and surfactant flow cases respectively. High air and low water flow rates were used in both instances. Substantial slug or even churning turbulent two-phase flow can be observed for the nonsurfactant flow in Figure 13. For the surfactant case large gas slugs are still present but there is no churning turbulence. In this case, however, the porous element had gross nonuniformity of the gas injection. This caused formation of large bubbles on the element. The nonuniformity of the gas injection was greatly reduced with the new element.

A separate set of tests were made using x-ray photography as a quantitative experimental method. These tests are listed in Table 2. Figures 15 and 16 are x-ray photographs of the two-phase flow in tests 21 and 22.

TABLE 2. AIR-WATER MIXING X-RAY TESTS

TEST NUMBER	AIR FLOWRATE		WATER FLOWRATE	SURFACTANT FLOWRATE
	$\frac{\ell}{s}$	$\frac{g}{s}$	$\frac{\ell}{s}$	$\frac{m\ell}{s}$
19	0.50	0.70	0.25	0
20	0.50	0.70	0.25	0.2
21	0.50	0.70	0.10	0
22	0.50	0.70	0.10	0.2
23	0.93	1.30	0.10	0
24	0.93	1.30	0.10	0.2
25	1.60	2.24	0.25	0
26	1.60	2.24	0.25	0.2
27	1.60	2.24	0.70	0
28	1.60	2.24	0.70	0.2

Each of these two Figures 15 and 16 represents superposition of forty individual flash x-ray exposures. In the non-surfactant case the x-ray negative appears texture-like. This is due to large temporal variations of the instantaneous void fractions across the channel. Another observation in the non-surfactant case, is increased void fraction within practically all wall boundary layers.

In the case of two-phase mixing with surfactant much more uniform and finer structure of the mixture is indicated by Figure 16. Increased void fractions can be observed only in the inner boundary layers on the trailing edge of the element. In the channel farther downstream the void fraction is quite uniformly distributed across and along the channel. Also the average void fractions appear higher than in the non-surfactant case. It is apparent from the x-ray and other photographs that surfactant induces a more desirable two-phase flow pattern for the purpose of efficient power conversion in LMMHD generators.

Degrees of shades of light at three locations: an inch and a half downstream of the elements trailing edge in Figures 15 and 16 were obtained by digital processing as described earlier. This data was then converted into local average void fractions across the channel as seen in Figs 17 and 18. The void fraction profile is more uniform and "smoother" in the test with a surfactant. Next to the injection surface void fraction reaches value of almost 0.9 while without surfactant the corresponding value is only 0.6. Surprisingly in the test without surfactant the void fraction has relatively high value near the outer boundary. Plausible explanation is given in below in discussion of the next two figures. From Figs 17 and 18 average void fraction across the channel can be evaluated. These are 0.55 for the non-surfactant flow and 0.8 for the surfactant flow.

Based on this data and the volumetric flow rates of air and water it was calculated that the average velocity slip ratios

$$S = \frac{u_a}{u_w} = \frac{Q_a}{Q_w}\left(\frac{1-\alpha}{\alpha}\right)$$

were S=4.1 and S=1.2 in the non-surfactant and the surfactant flow ases respectively. A very significant reduction in the slip ratio was achieved.

It is very interesting to observe void fraction distributions around the injection element itself. These are given on Figures 19 and 20 for tests 19 and 20. Surprisingly in the non-surfactant case (when bubbles are considerably larger) the boundary layer is substantially thinner than in the surfactant case. Also, in the non-surfactant case voids (bubbles) appear to distribute much more abruptly across the two side channels and even accumulate in the outer boundary layers. Possible large (or small) scale turbulence being convected from the region upstream of the injection element does not appear to be a likely cause (it is likely that this kind of turbulence is too weak) as it would act equally in the surfactant case as well. It is speculated that shear layer turbulence generated at the injection boundaries is the cause of the void fraction redistribution phenomena. It appears that this turbulence is much stronger in the non-surfactant case. This could be due to a stronger perturbing effect in terms of velocity differential of larger gas bubbles as they grow on the injection surface. After detachment many of these bubbles appear to be carried by large eddies and "splashed" against the opposite wall. These bubbles appear to "remain" there for some period of time creating an increased void fraction boundary layer. This is not the case with the surfactant flow. Bubbles detach from the injection wall more readily at much smaller sizes. They are carried along the flow much more easily without an appreciable slip or drag force. Thus, much less or no turbulence is created. This also means that for the surfactant case less energy is dissipated in mixing. The small bubbles probably even damp out turbulence which would exist if single phase liquid boundary layers were present. This discussion of the effects of turbulence on void fraction distribution is substantially valid for higher flowrates as well.

Observation of the flow a short distance downstream of the injection element in Figures 19 and 20 shows that much more uniform void fraction distribution is obtained in the surfactant case. This will be, of course, of utmost importance for subsequent MHD power conversion in the case of two-phase liquid metal flow.

Table 2 indicates that x-ray photographs were obtained for ten tests with the last injection element which had satisfactory uniform gas injection. The x-ray negatives have been processed digitally and void fractions have been obtained presently only for tests 21 and 22 (Figs 17 and 18). The intention was to process digitally all ten cases. However, the frame grabber board of the processing equipment has failed and is being repaired. This is the reason why other void fraction profiles are not reported for the last (the best) injection element.

f. Application of Air-Water Mixing Results

The goal of the air-water mixing experiments was to confirm design principals for a larger N_2-NaK mixer prototype capable of creating high void fraction homogenous bubbly flow with low slip velocity. Visual and especially x-ray photographs have proven to be a very powerful experimental tool for qualifying and quantifying results. However these methods still cannot precisely quantify transition from bubbly to patchy (large bubbles) gas injection.

The surfactant appears to be an important factor in the control of the resulting void fractions. Most important is that surface activity prevents coalescence of bubbles in the bulk of flow thus preventing formation of a slug flow pattern. Our observations also indicate that the surface activity shifts, to some degree, transition from bubbly to patchy gas injection toward higher injection rates. We have also found that the presence of a surfactant drastically reduces the size of bubbles generated.

A second important controlling variable is the gas injection velocity through a porous plate. There is some "critical" injection velocity at which transition from bubbly to patchy gas formation occurs. In reference 4 injection of air through a porous bottom into a stagnant liquid column had been investigated. When a surfactant was used in that study the observed critical injection velocity was at about 0.046 m/s or mass flux about 0.053 kg/m^2s. A third influential variable is the incoming liquid velocity parallel to the injection surface. We have not investigated quantitatively the effect of the

liquid velocity. However it is known that in forced boiling a ten fold increase in the liquid velocity results in an increase of the "critical" heat flux by about a factor of two. Since our gas injection is fluid dynamically similar to boiling we could expect about the same influence of the liquid velocity. A fourth influential factor probably is the void fraction in the incoming flow. If the incoming flow, to a particular porous plate injection location, is of high void fraction then it is likely that the critical injection velocity will be lower. This is known to be the case in boiling as well. The reason is that there is less liquid available to come to the surface and take away newly injected bubbles. Uniformity of the gas injection is important of course as well. Nonuniform gas injection may have local injection velocities higher than critical.

Nominal pore size for the last few gas injection elements was 0.5 microns. Elements with pore sizes of 5 and 2 microns have been tried earlier. They led to low pressure drop across the porous plate which resulted in nonuniform distribution of the air injection rate. This was the reason that plates of porosity 0.5 microns were ultimately used. The plate of 0.5 microns porosity had a pressure drop of 1 to 6 PSID which was sufficient to ensure uniformity of injection.

In the range of our experiments the size of the pores does not appear to make noticeable effect on size of generated bubbles. This is probably so because the pores are much smaller than the bubbles. In the surfactant flows, generated bubbles were about 0.2 millimeters in diameter, while in the surfactant flow they were 2 to 3 millimeters in diameter.

These experiments also verified that the two-phase flow separation downstream of the injection element can be completely eliminated. This is important since a separated region can serve as a source of large gas slugs.

In the large N_2-NaK mixer prototype the gas injection velocity will be kept safely below the critical velocity in order to ensure bubbly injection. Also separation downstream of the injection elements will be avoided. Our present plan involves mixing of N_2 and NaK at higher pressures. This will mean smaller

gas volumes so that the size of the injection surface will not have to be very extensive. A different surfactant will definitely be used with NaK than with water. A surfactant will be chosen based on existing knowledge or by performing small bubbling experiments in NaK.

Due to the very short residence time of two-phase flow in a LMMHD generator and the need for subsequent NaK separation, only a weak transient forming surfactant is needed. Since no persistent forming could be used with a liquid metal, other foam generating mixing concepts will not work in our application. These concepts are for example beating and shaking of two phases or passing it through a steel wool packing. These concepts work only for persistent foams and are too energy consuming as well.

g. Liquid-Metal MHD Blowdown Loop

The key part of this experimental program is testing with the Liquid-Metal MHD Blowdown Loop. A used Varian electromagnet with the necessary power supply and cooling system has been obtained. The poles are one foot in diameter. For a two-inch air gap the strength of the magnetic field is 1.3 Tesla. Other components of the system which have been obtained are two large stainless steel tanks. Each has a capacity of 300 gallons and boiler certification ratings of 1000 psig. One of the tanks will be used for high-pressure liquid-metal supply while the other will be used for two-phase flow separation. The high-pressure supply tank will allow mixing at high pressure and thus large expansion pressure ratio (possibly up to 50) through the nozzle and the MHD generator. These kinds of experiments have not been done before. If the mixing is accomplished at high pressure, the volume of the gas and void fractions are much lower. This makes it much easier to generate homogeneous bubbly flow in a mixer. Rapid pressure drop and large expansion of much bubbly flow could create significant additional surface active effects which would extend the life of transient foam. Namely, rapidly expanding gas within the bubbles would cool very rapidly thereby appreciably lowering temperature of their liquid metal interface. Thinner parts of the liquid lamina would temporarily have a temperature lower than their thicker parts. This could cause surface tension of the thinner parts to be higher than surface tension of the thicker parts. This is practically identical to the manner in which a surface actively induces

interfacial boundary layer flow which temporarily prevents coalescence of bubbles and extends the lifetime of the bubbles.

A layout of the Liquid Metal MHD Blowdown Loop is given in Figures 21, 22, and 23. High pressure (up to 1000 psig) liquid metal (NaK) from the supply tank flows into the mixer where it is mixed with high pressure nitrogen. The two-phase mixture subsequently flows through a nozzle and a MHD generator. Main separation of the two phases is accomplished in the swirl separator. However, the nitrogen exiting the swirl separator might still be carrying over some liquid metal droplets. This mixture is then introduced into the large separation tank (300 gallons) where vanes introduce swirling flow which separates the remaining liquid drops. The nitrogen is, subsequently exhausted into the atmosphere. There should be no liquid metal carryover in the exhausting gas. However, should the carryover accidentally occur it will be detected by electrical conductivity probes located within the liquid metal trap set up in the exhaust system.

The flow in the mixer and the MHD generator is vertically upwards. This means that there will be no problems with two-phase flow separation during the start-up. It is expected that steady state blowdown operation will be established within 10 seconds. A blowdown run should last a minute or two. Return of the liquid metal from the separation into the supply tank will be done afterwards using pressurization and a small return pipe.

New pole pieces have been designed for the magnet. They are shaped to provide maximum magnetic flux density throughout the generator. Detailed design of the experimental test section has been completed. This includes inlets for the liquid metal and the gas, the flow straightening section for the liquid metal, the mixer, the two-phase flow nozzle the LMMHD generator, and the generator exit section. The actual inner shape of the generator will be determined when the exact distribution of the magnetic flux lines becomes known after installation of the new magnet pole pieces has been completed and shakedown tests have been made.

ACKNOWLEDGEMENTS

The research described in this report was performed by the Jet Propulsion Laboratory, California Institute of Technology. The AMTEC work was supported by the Energy Conservation and Utilization Technologies Program (ECUT), Office of Energy Utilization Research, Department of Energy, and by the National Aeronautics and Space Administration (NASA). The work on LMMHD was supported exclusively by ECUT.

REFERENCES

1. P. F. Massier, C. P. Bankston, G. Fabris and L. D. Kirol, "ECUT Direct Conversion Technology Annual Summary Report CY 1988", JPL D-5698, Jet Propulsion Laboratory Pasadena, California, December 1, 1988.

2. P. F. Massier, "ECUT Direct Conversion Technology Annual Summary Report CY 1987", JPL D-4856, Jet Propulsion Laboratory, Pasadena, California, January 7, 1988.

3. P. F. Massier, "ECUT Direct Conversion Technology Project Annual Report CY 1986", JPL D-3707, Jet Propulsion Laboratory, Pasadena, California, January 15, 1987.

4. G. B. Wallis, "Some Hydrodynamic Aspects of Two-Phase Flow and Boiling", International Developments in Heat Transfer. American Society of Mechanical Engineers, Paper No. 38, Vol. 2, pp 313-340, 1961.

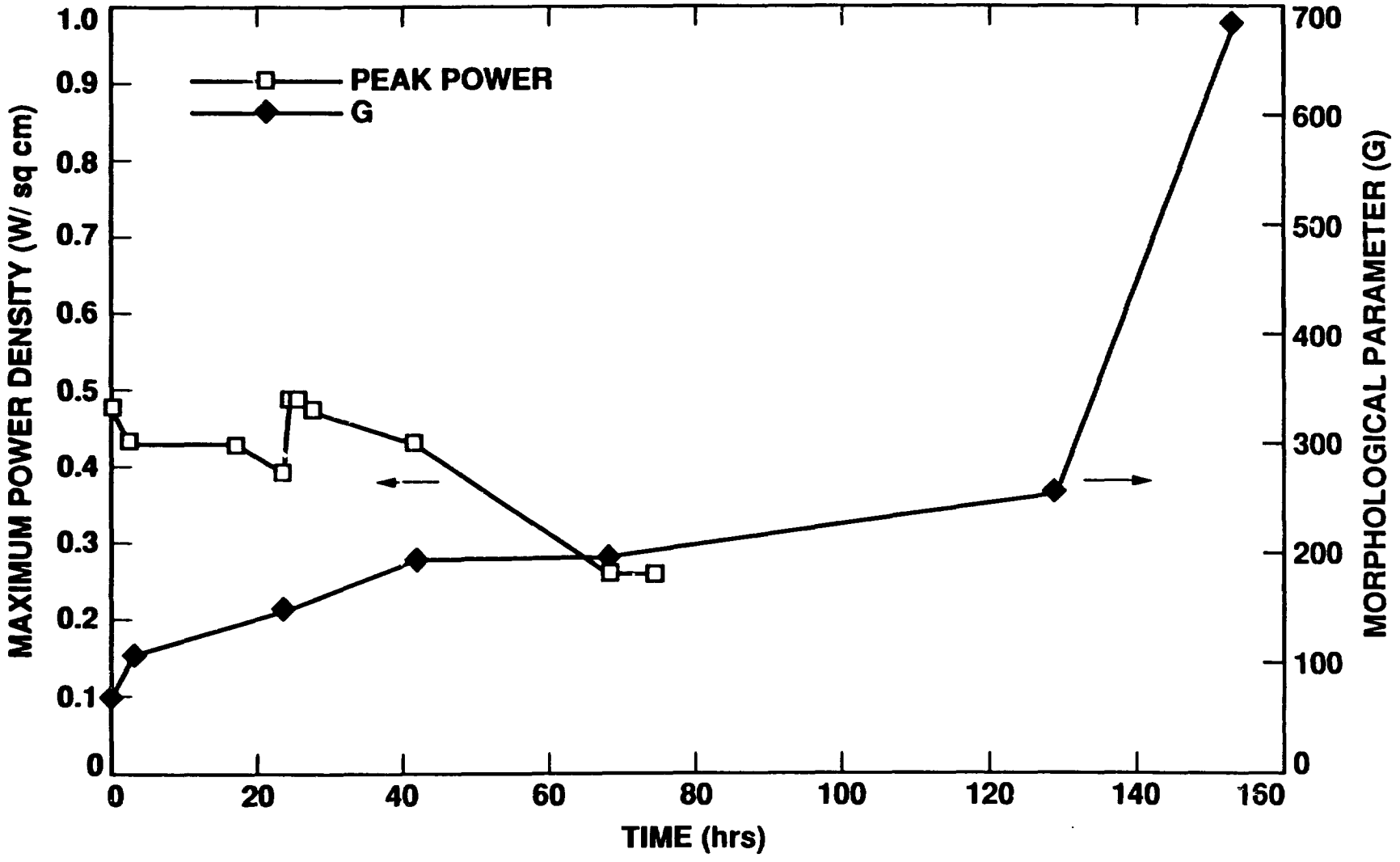

Figure 1. Maximum Power Density for TiN Electrodes

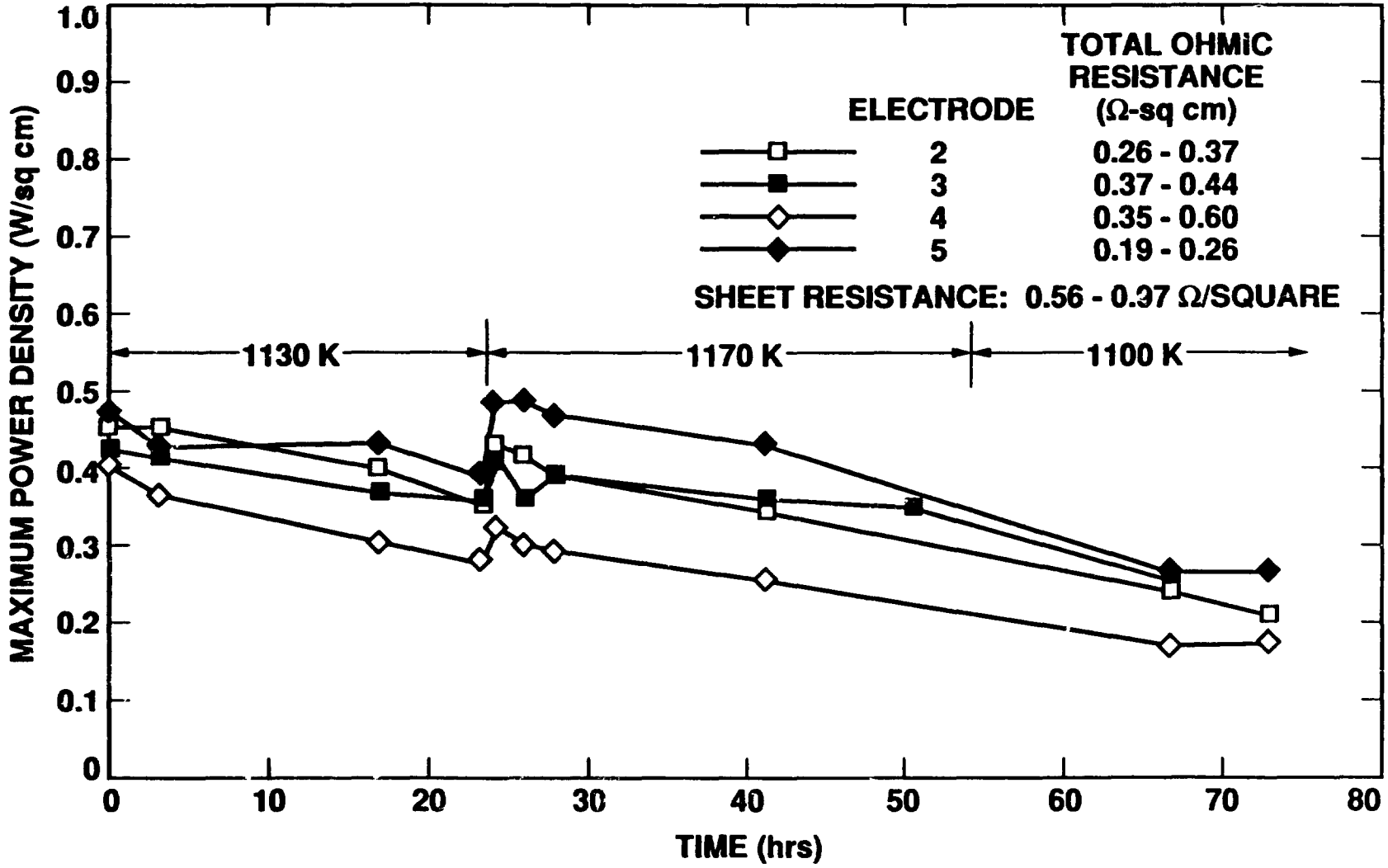

Figure 2. Change of Morphological Parameter and Power Density with Time

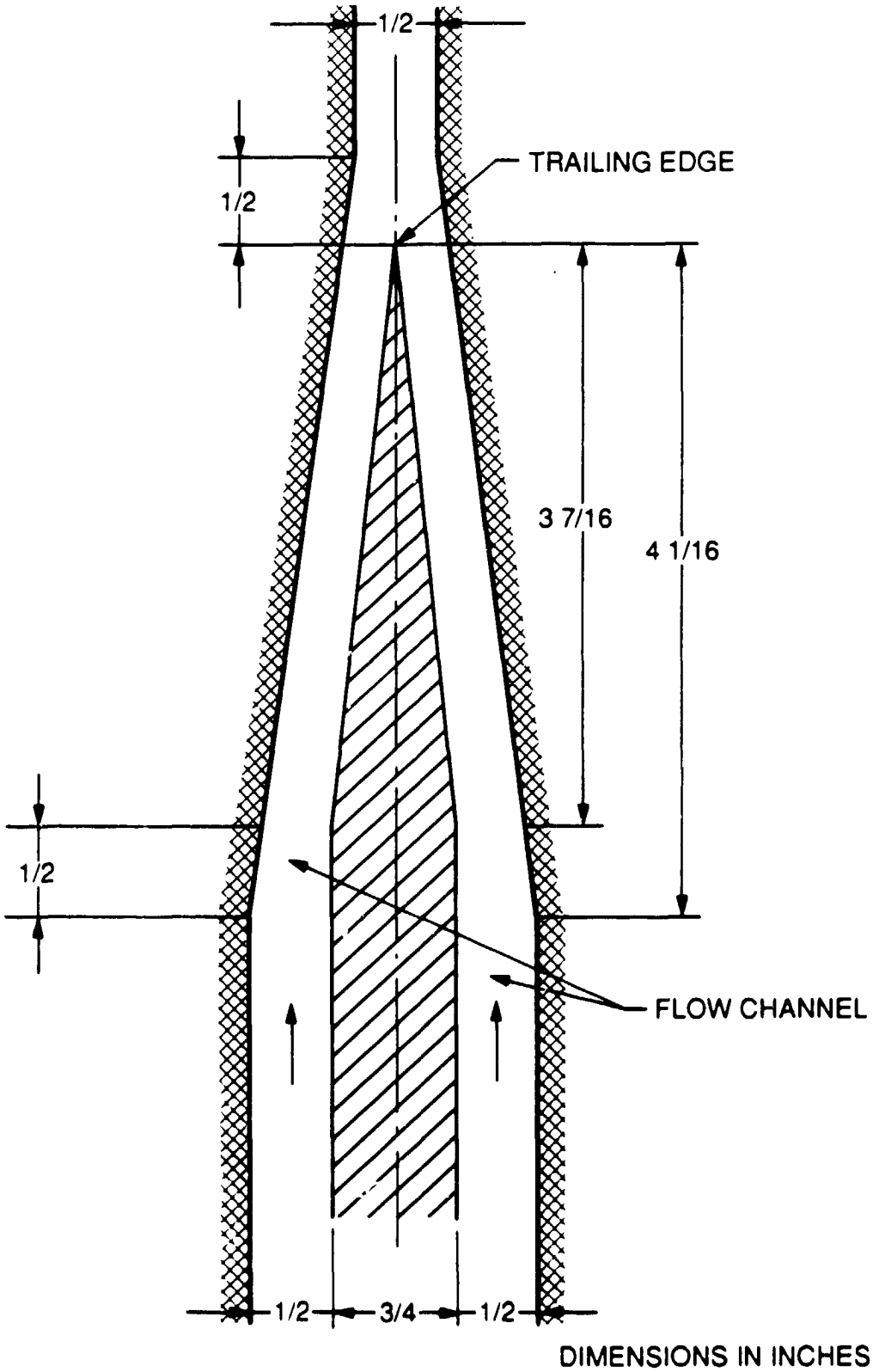

Figure 3. Dimensions of Gas-Water-Soap Mixing Test Section

Figure 4. X-Ray Photo Negative
of the Stepwedge Calibration

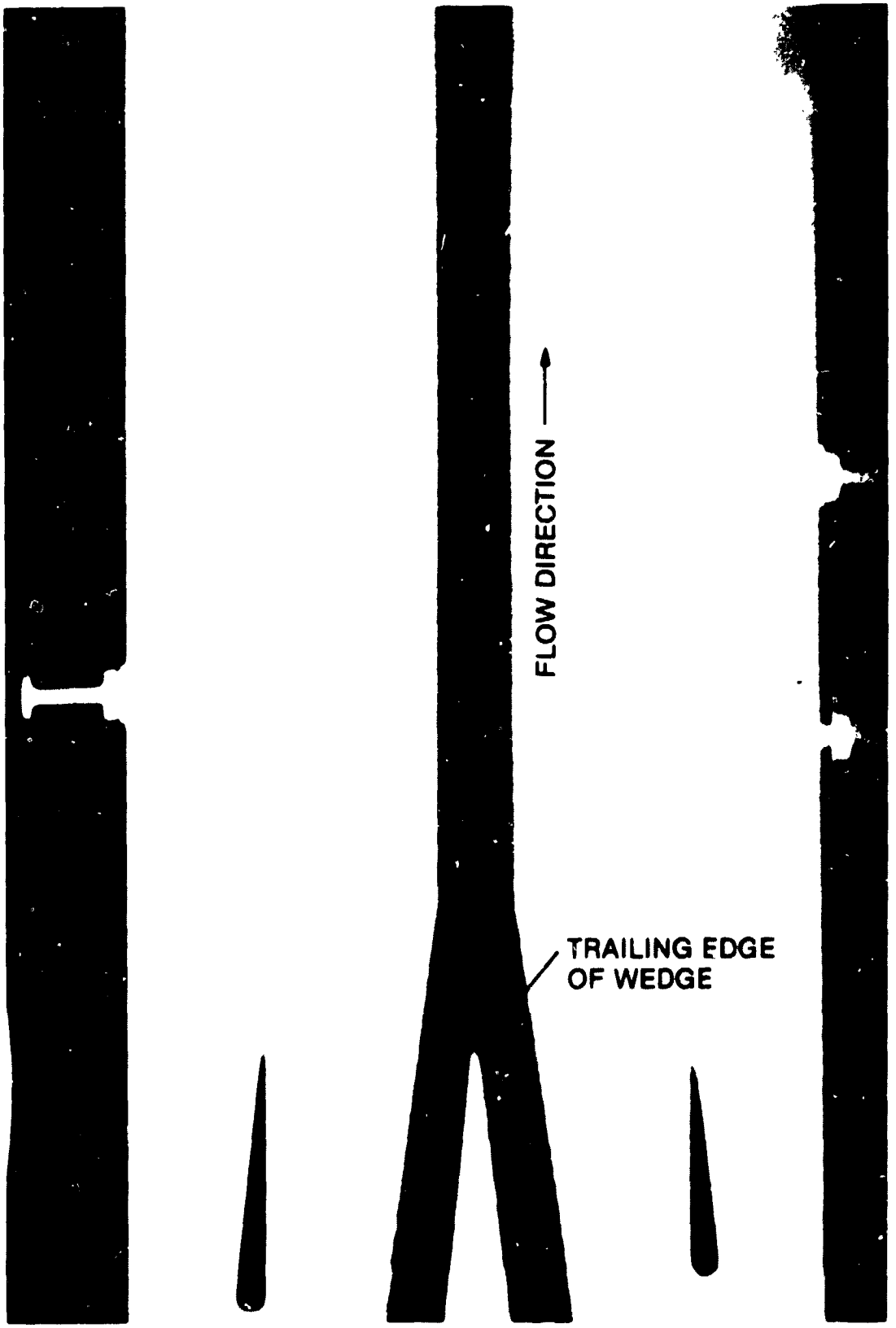

Figure 5. Typical X-Ray Photo of Two-Phase Flow.
Ten Flash X-Ray Exposures Superimposed

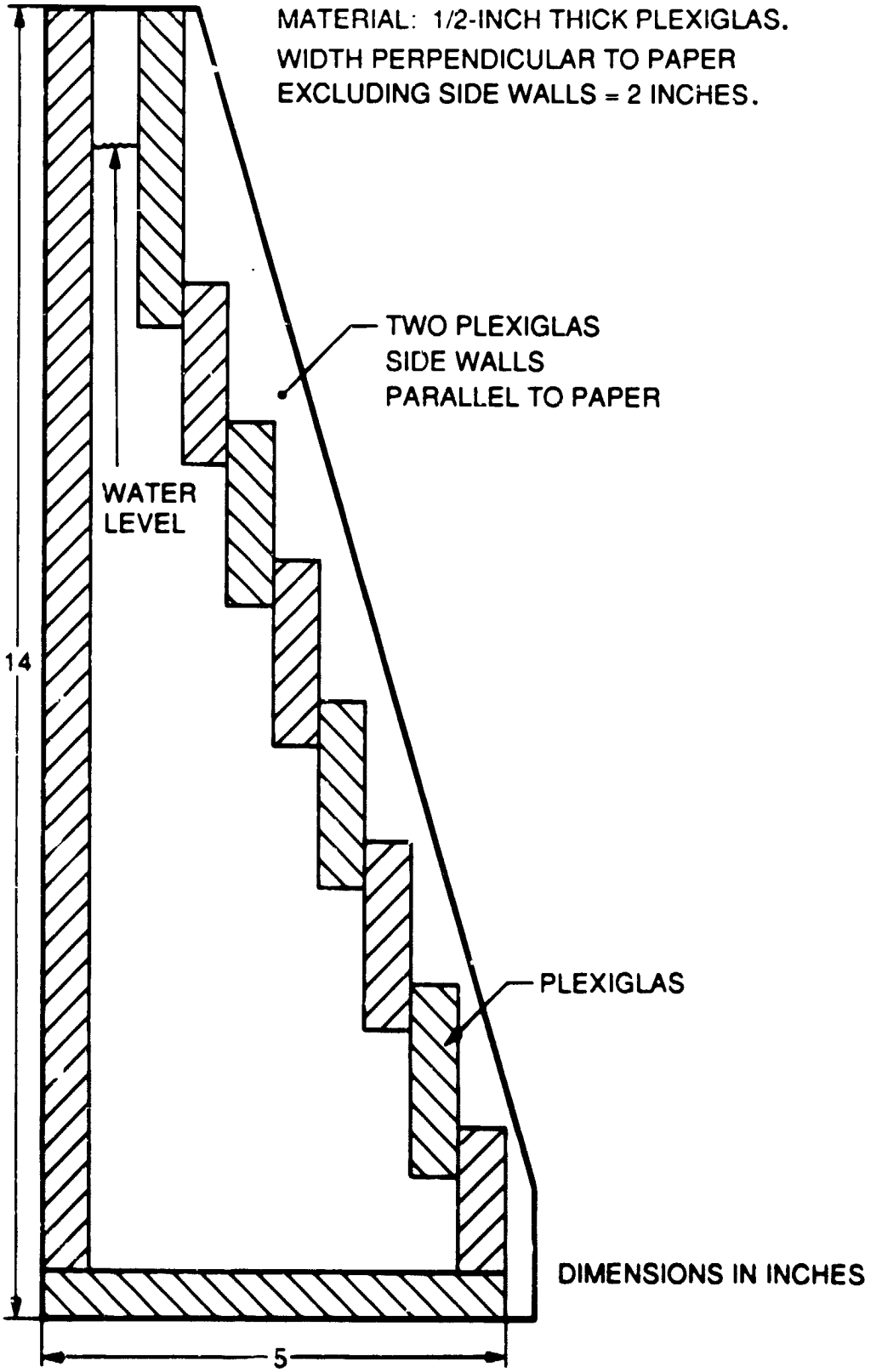

Figure 6. Calibration of Stepwedge for Void Fractions

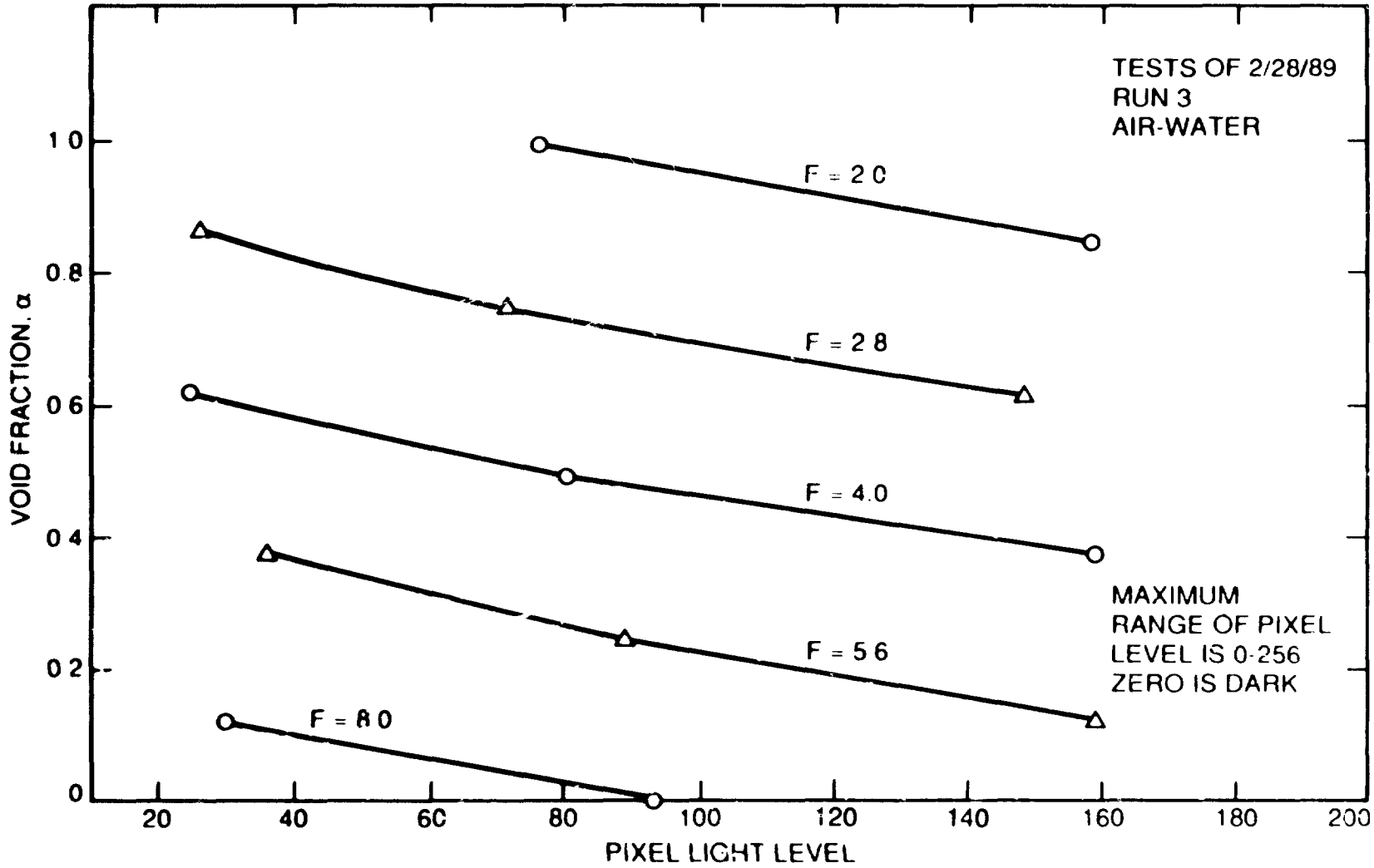

Figure 7. Void Fraction Versus Pixel Light Level

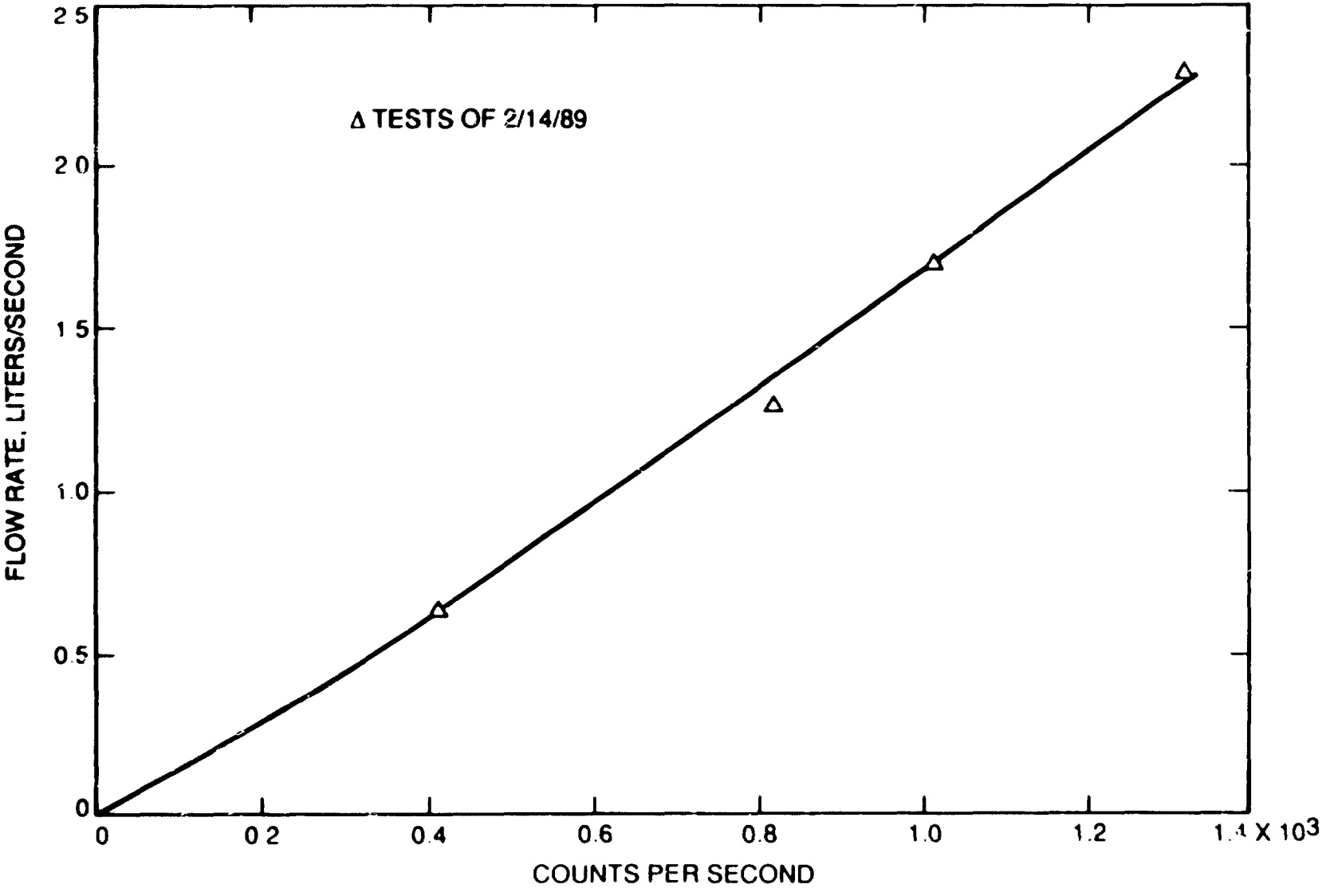

Figure 8. Calibration of Turbine Flow Meter

Figure 9. Air-Water Test with Low Air and Low Water Flowrates

Figure 10. Air-Water-Soap Test with
Low Air and Low Water Flowrates

Figure 11. Air-Water Test with Low Air and Low Water Flowrates

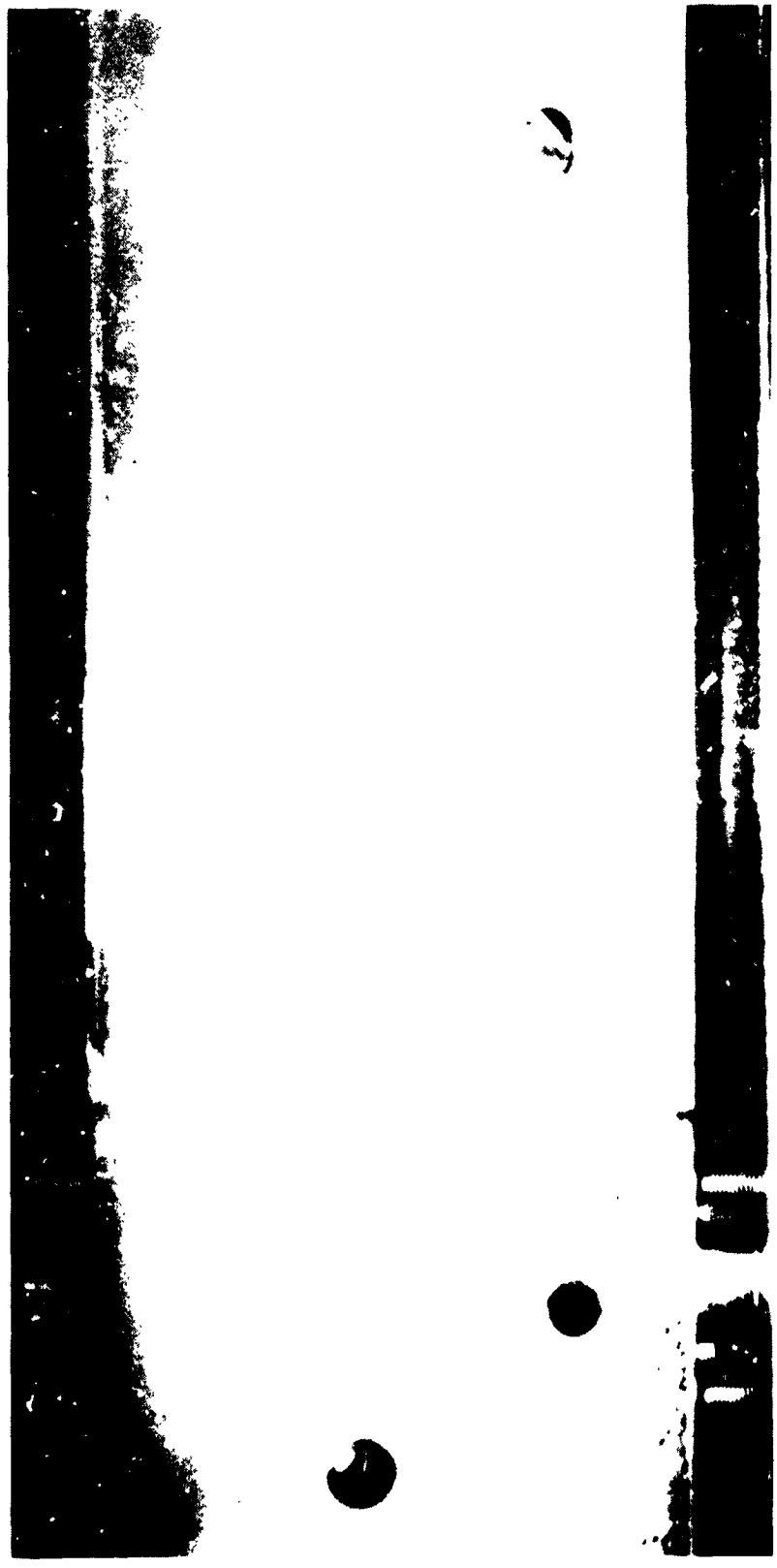

Figure 12. Air-Water-Soap with
Low Air and Low Water Flowrates

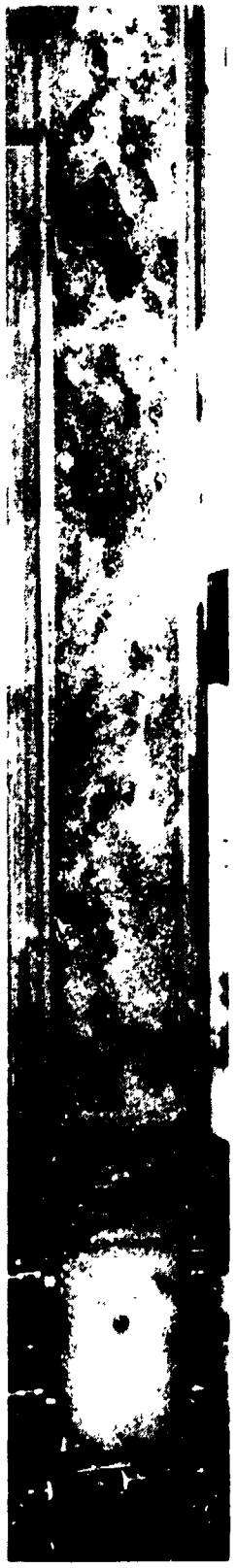

Figure 13. Air-Water Test Showing Whole Channel View with High Air and Low Water Flowrates

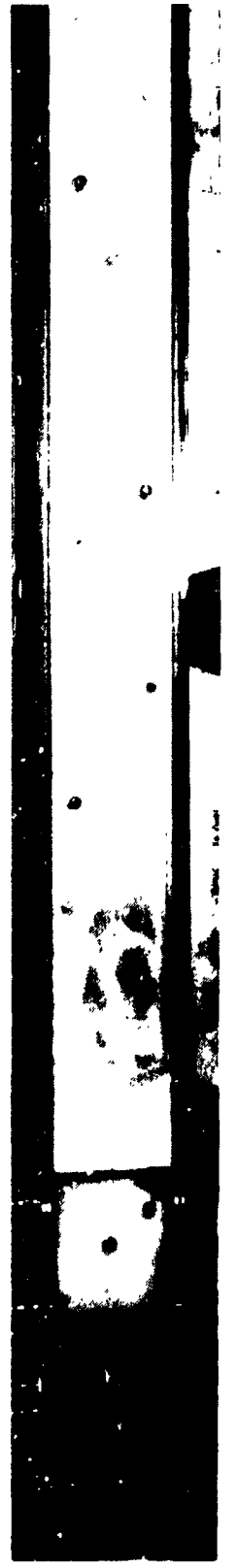

Figure 14. Air-Water-Soap Test Showing Whole Channel View with High Air and Low Water Flowrates

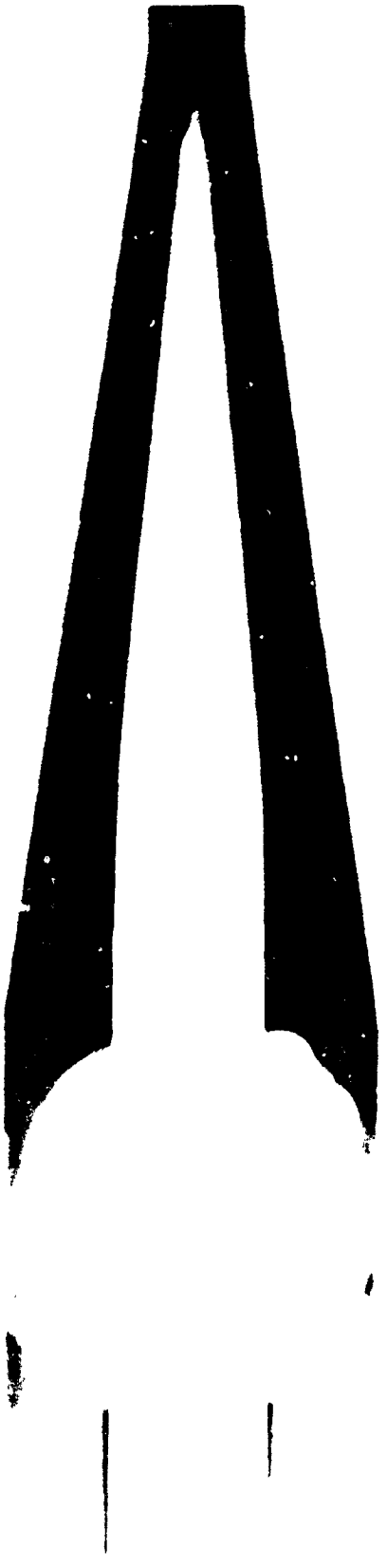

Figure 15. X-Ray Photo of Air-Water Test at Flowrates of 0.5 and 0.1 l/s Respectively.

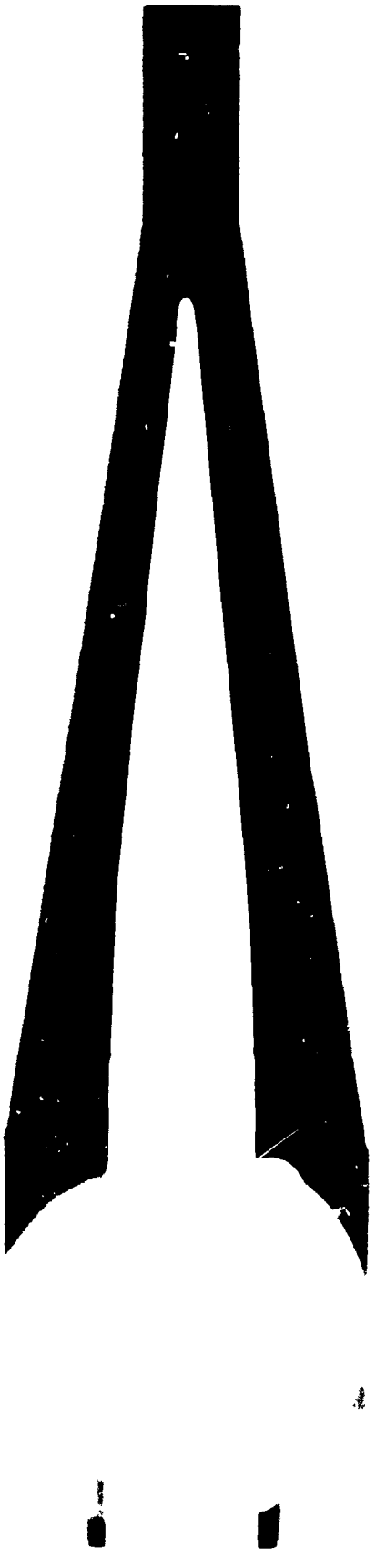

Figure 16. X-Ray Photo of Air-Water-Soap Test at Flowrates of 0.5 and 0.1 l/s and 0.2 ml/s Respectively.

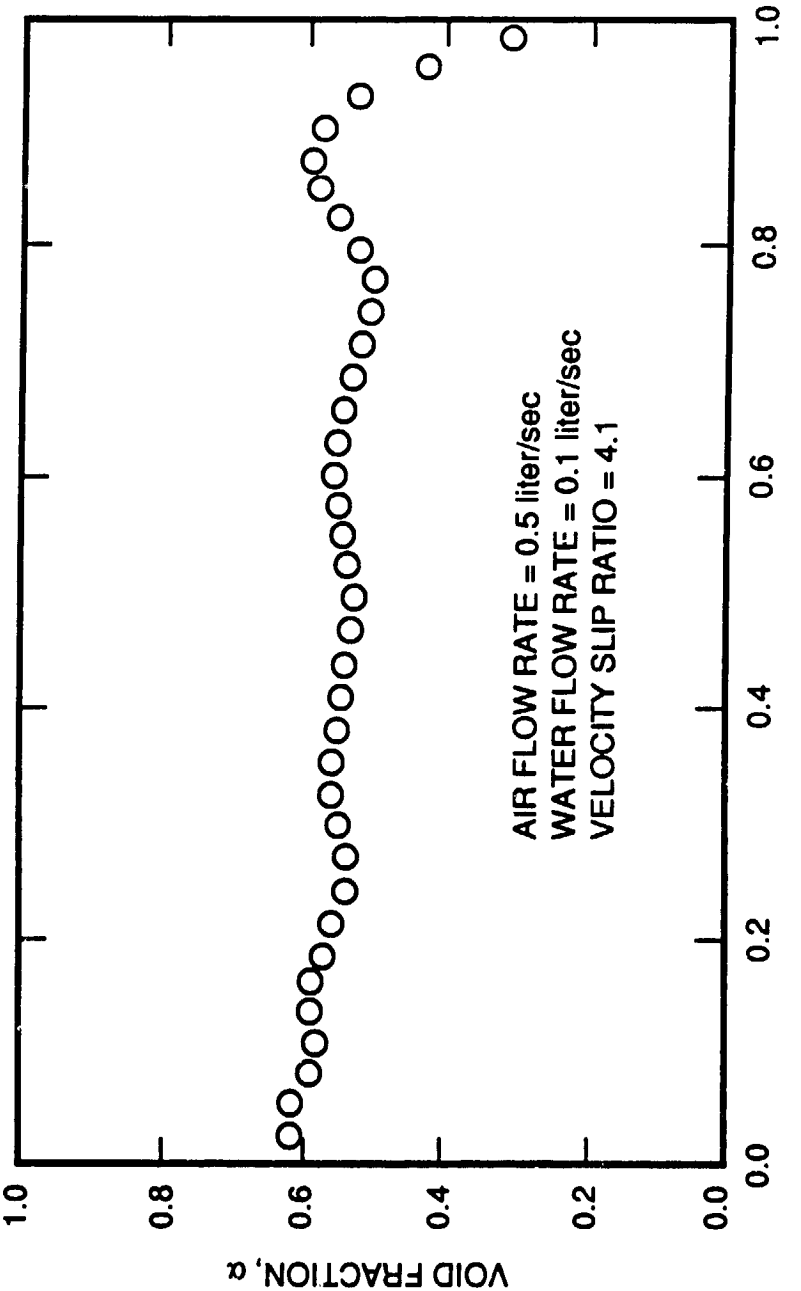

FIGURE 17. VOID FRACTION FOR AIR/WATER MIXTURE WITHOUT SURFACTANT

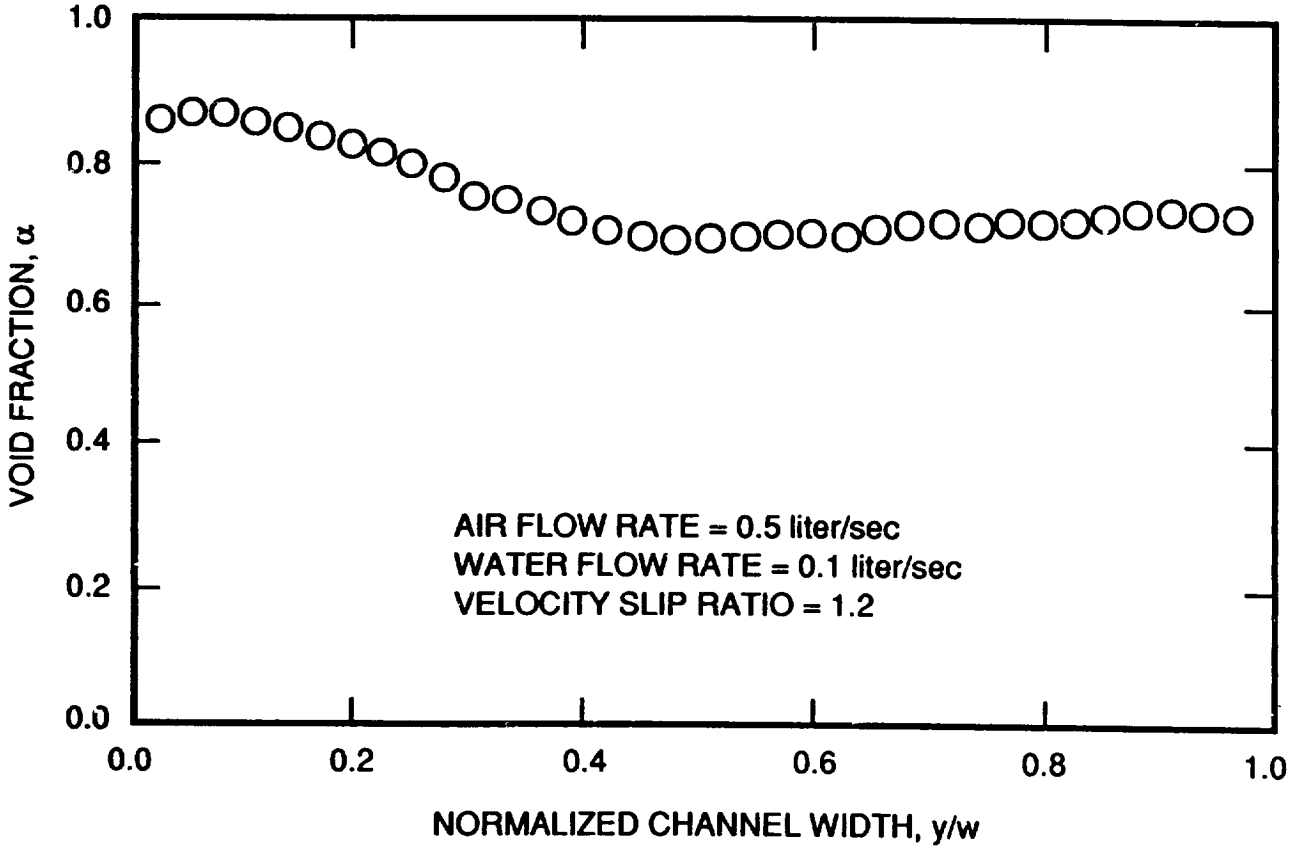

FIGURE 18. VOID FRACTION FOR AIR/WATER MIXTURE WITH SURFACTANT

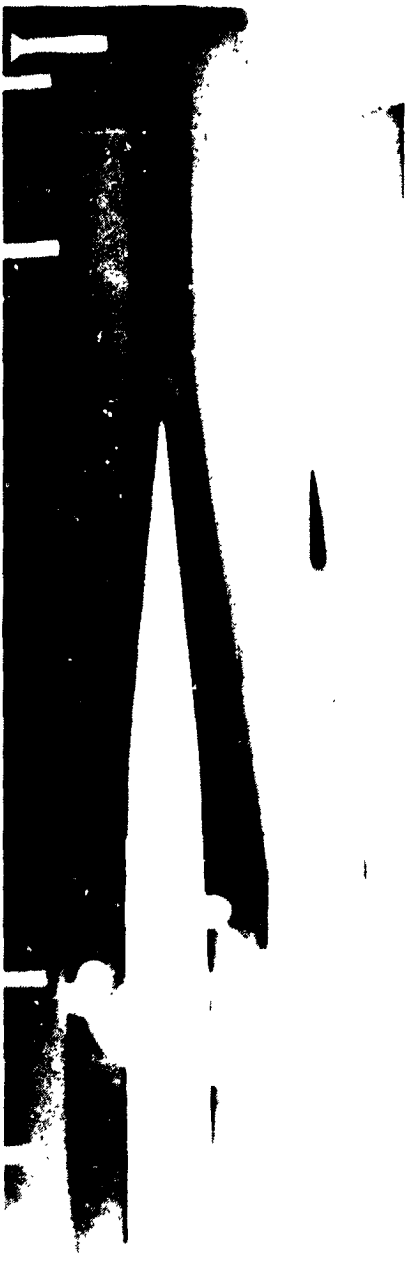

Figure 19. X-Ray Photo Showing Injection Element for Air-Water Test with Medium Air and Low Water Flowrates

Figure 20. X-Ray Photo Showing Injection Element for Air-Water-Soap Test with Medium Air and Low Water Flowrates

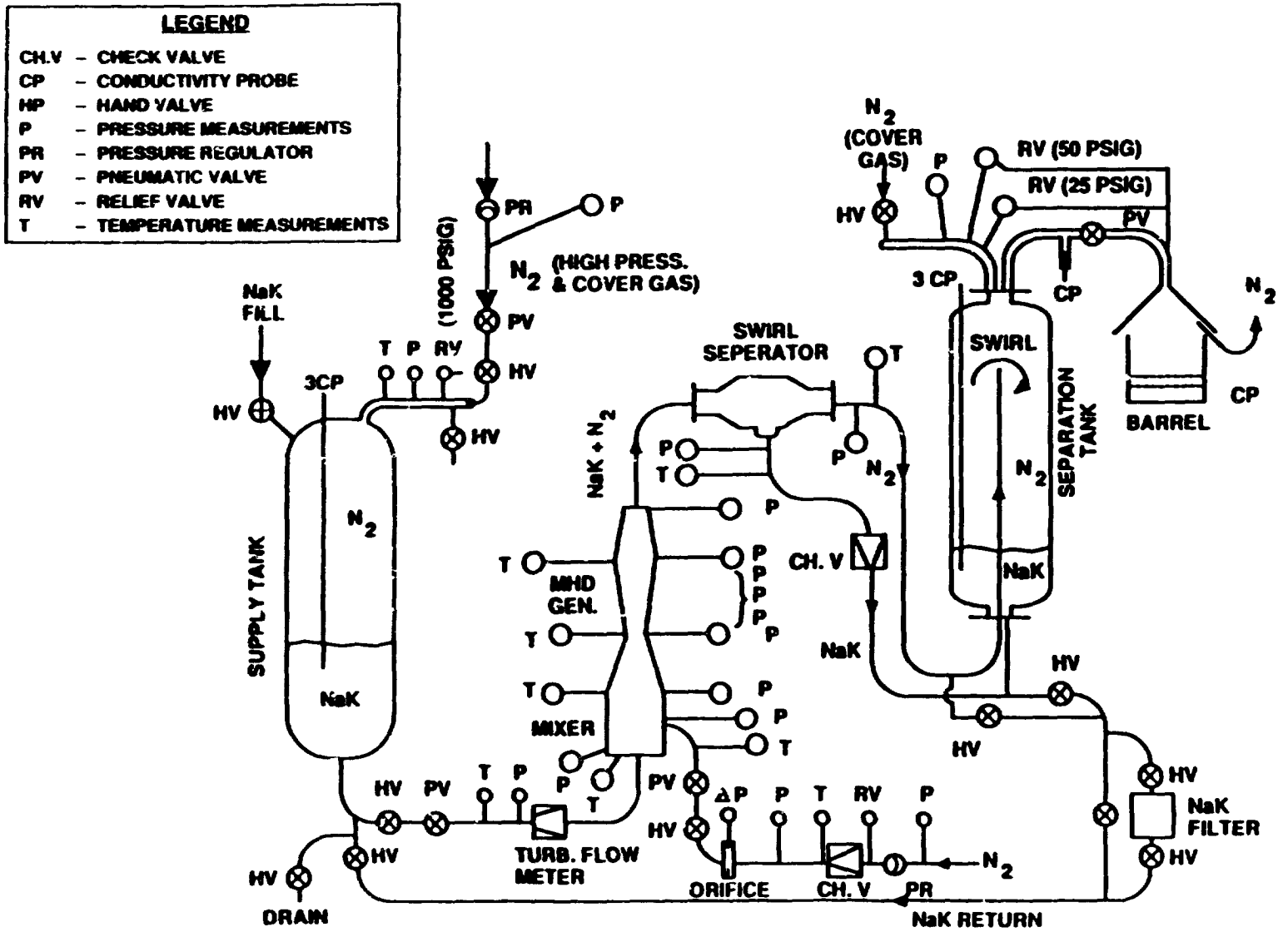

FIGURE 21. LIQUID-METAL MHD BLOWDOWN LOOP

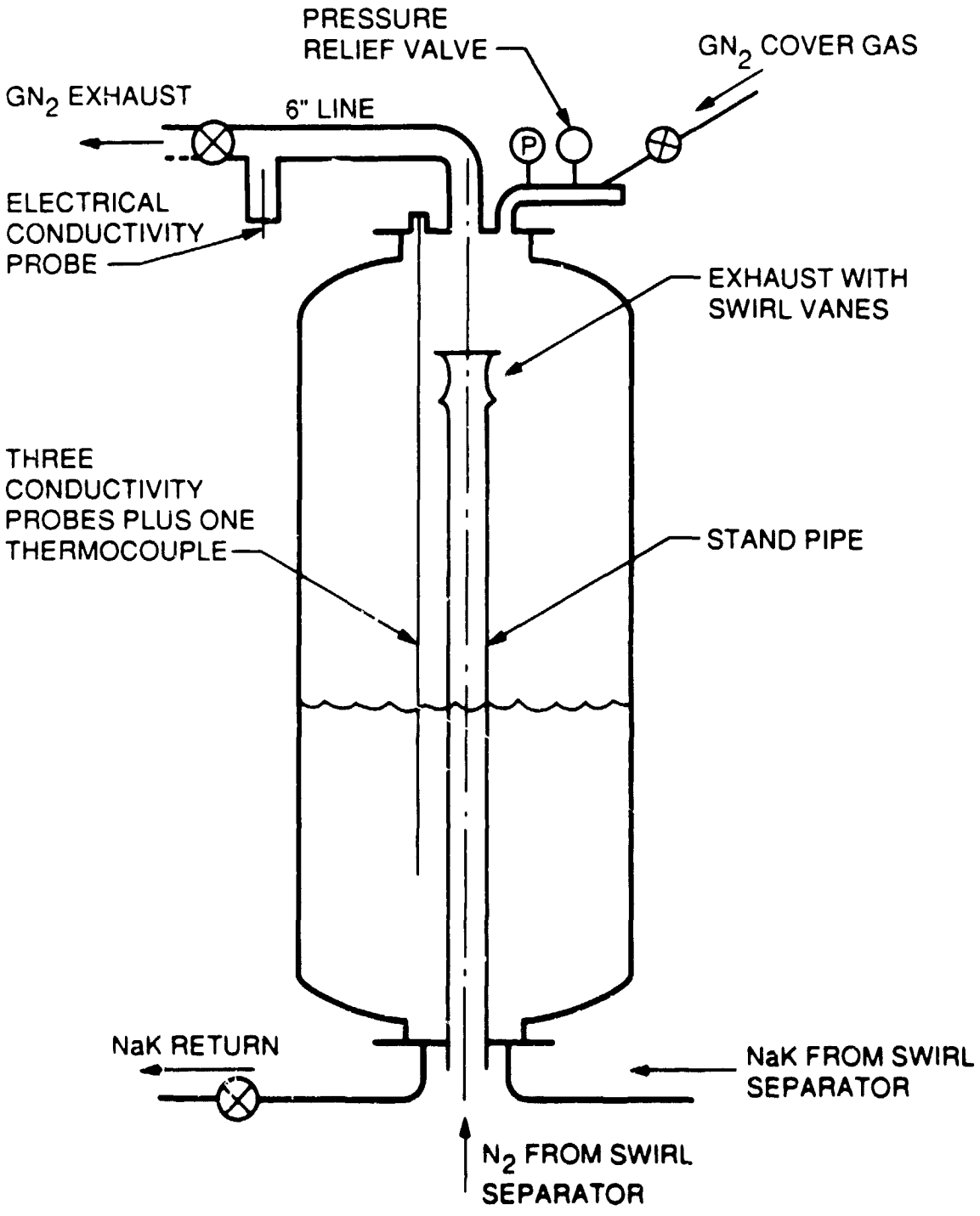

Figure 22. Separator Tank of the LMMHD Blowdown Loop

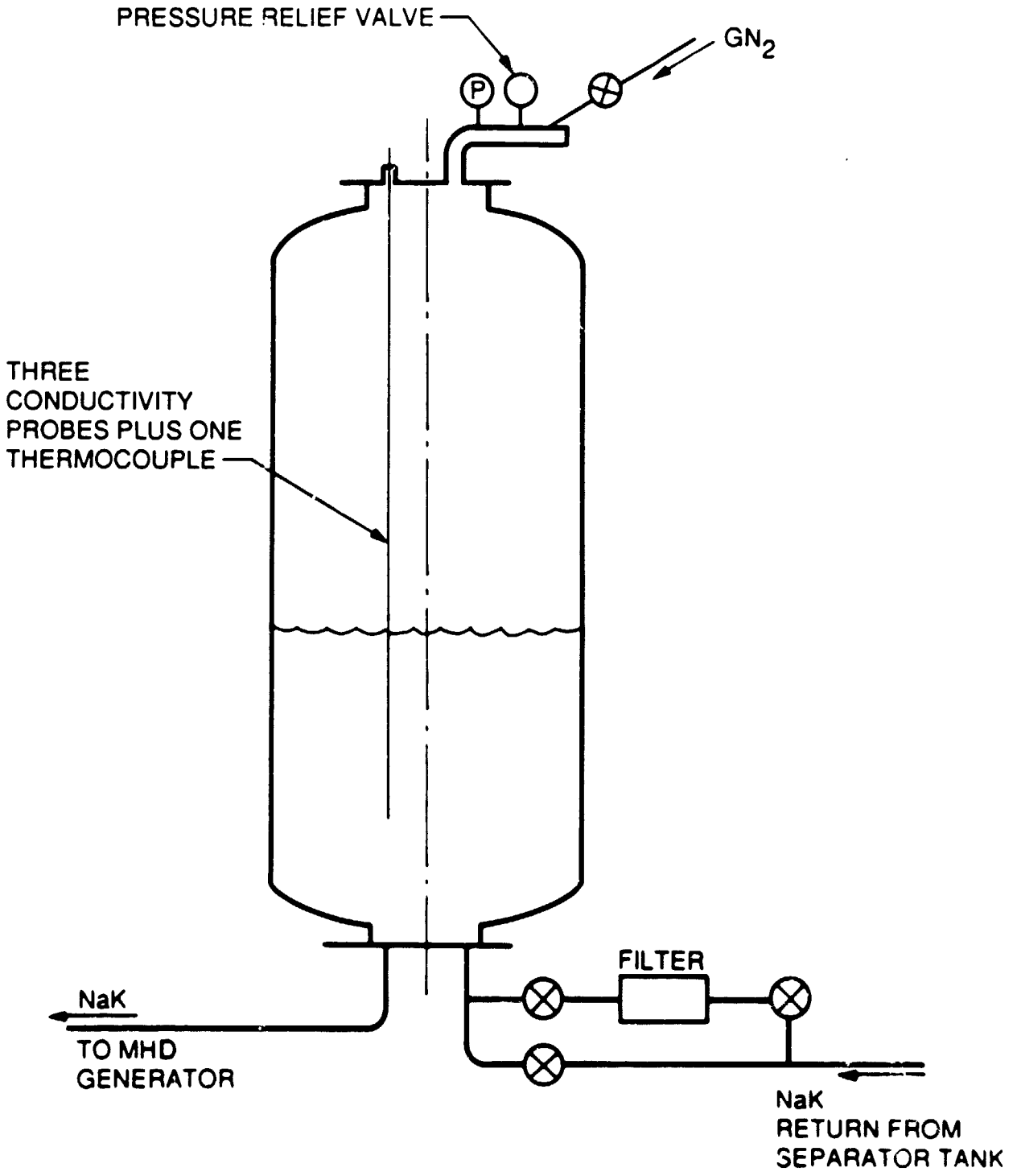

Figure 23. Liquid Metal Supply Tank of the LMMHD Blowdown Loop

APPENDIX A

Abstracts of Papers on AMTEC Presented at the May 1989 Meeting of the Electrochemical Society

1. M. L. Underwood, R. M. Williams, B. Jeffries-Nakamura, and C. P. Bankston, of the Jet Propulsion Laboratory; and N. Weber and G. Harkins, of Cermatec, Inc., and Beta Power, Inc., "Characteristics of Titanium Nitride Electrodes for AMTEC".

2. R. M. Williams, B. Jeffries-Nakamura, M. L. Underwood, and C. P. Bankston of the Jet Propulsion Laboratory, "Kinetics and Transport at the Sodium Beta Alumina/Porous Metal Electrode Interface".

Preprints Removed

APPENDIX B

Performance of WPt and WRh Electrodes in AMTEC

1. R. M. Williams, B. Jeffries-Nakamura, M. L. Underwood, B. L. Wheeler, M. E. Loveland, S. J. Kikkert, J. L. Lamb, T. Cole, and C. P. Bankston, "High Power Density Performance of WPt and WRh Electrodes in the Alkali Metal Thermoelectric Converter," Journal of the Electrochemical Society, Vol. 136, No. 3 March 1989, pp. 893-894.

Reprint Removed

APPENDIX C

Mass Transport, Charge Transfer and Ohmic Losses in AMTEC

1. R. M. Williams, B. Jeffries-Nakamura, M. L. Underwood, M. E. Loveland, T. Cole, and C. P. Bankston, "Mass Transport, Charge Transfer, and Ohmic Losses in the Alkali Metal Thermoelectric Converter", Industrial Chemical Engineering Symposium Series No. 112, The Institution of Chemical Engineers, Rugby, UK, pp. 153-163, 1989.

2. R. M. Williams, M. E. Loveland, B. Jefferies-Nakamura, M. L. Underwood, C. P. Bankston, H. Leduc and J. T. Kummer, "Kinetics and Transport at AMTEC Electrodes, I. The Interfacial Impedance Model", manuscript prepared but not included herein.

3. R. M. Williams, B. Jefferies-Nakamura, M. L. Underwood, C. P. Bankston and J. T. Kummer, "Kinetics and Transport at AMTEC Electrodes, II. Temperature Dependence of the Interfacial Impedance of $Na_{(g)}$/Porous Mo/Na - Beta" Alumina", manuscript prepared but not included herein.

Preprints Removed

APPENDIX D

AMTEC Recirculating Test Cell Component Testing and Operation

1. M. L. Underwood, R. K. Sievers, D. O'Connor, R. M. Williams, B. Jeffries-Nakamura, and C. P. Bankston, "AMTEC Recirculating Test Cell Component Testing and Operation," will appear in the Proceedings of the Intersociety Energy Conversion Engineering Conference (IECEC) during August, 1989.

Preprint Removed